



Rapid Joule heating-induced welding of silicon and graphene for enhanced lithium-ion battery anodes

Fan Yang^{a,1,*}, Pengcheng Deng^{a,1}, Hang He^{a,1}, Ruolan Hong^a, Kun Xiang^b, Yuan Cao^a, Beibei Yu^a, Zeman Xie^a, Jiming Lu^c, Zikang Liu^a, Danish Khan^a, David Harbottle^d, Zhenghe Xu^e, Qingxia Liu^{a,*}, Zeguo Tang^{a,*}

^a College of New Materials and New Energies, Shenzhen Technology University, Shenzhen 518118, PR China

^b Hangzhou Hikvision Digital Technology Co. Ltd., Hangzhou 310051, PR China

^c School of Resource & Environment, Hunan University of Technology and Business, Changsha 410205, PR China

^d School of Chemical and Process Engineering, University of Leeds, Leeds LS2 9JT, UK

^e College of Engineering, Southern University of Science and Technology, Shenzhen 518055, PR China

ARTICLE INFO

Keywords:

Silicon-based anode
Energy storage material
Lithium-ion batteries
Joule heating
Silicon carbide
Welding

ABSTRACT

In the pursuit of enhanced energy storage solutions, the application of silicon-based anode materials faces significant hurdles, primarily stemming from the rapid capacity degradation during battery cycles. This study introduces a novel and efficient method for fabricating Si/graphene composites (F-Si@rGO), enhancing the performance and longevity of silicon-based anodes. Utilizing ultra-high-speed thermal treatment, this technique controls the thermal interaction between carbon and silicon phases, leading to the formation of silicon carbide “riveting points” that firmly anchor silicon nanoparticles within the graphene matrix. This novel method effectively minimizes the problems of phase segregation, which are caused by varying degrees of wettability alteration in the two phases during conventional heat treatments, and guarantees a robust integration of graphene and silicon. This integration results in homogeneous charging and outstanding structural stability of the composites, over extended cycles of use. The resulting Si/graphene composites exhibit exceptional electrochemical performance, achieving a high initial capacity of 1141.3 mAh g⁻¹ at 1C and maintaining a capacity of 894.95 mAh g⁻¹ after 1000 cycles with minimal degradation (0.0216 % per cycle). This synthesis method, notable for its speed and scalability, offers a potential advancement in battery material technology, suggesting a path towards more resilient and efficient energy storage solutions.

1. Introduction

The state of the art graphite-based anodes can reach an energy density of 360 ~ 365 mAh g⁻¹, which is very close to the theoretical specific capacity of graphite at 372 mAh g⁻¹ [1]. Further improvements on the overall energy density of the battery packs shall rely heavily on developing new cathode and anode materials. Silicon-based anode materials offer great promise for the next-generation high-density lithium-ion batteries due to their exceptionally high theoretical specific capacity (3580 mAh g⁻¹ at room temperature), low delithiation potential (< 0.5 V), environmental sustainability and ample availability in the earth's crust [2]. However, the widespread commercial utilization of silicon-based anodes is often hindered by their rapid capacity degradation

during battery cycling [3]. When silicon undergoes lithiation, it experiences significant swelling, leading to the fragmentation of silicon particles and the continuous formation of solid-electrolyte interface (SEI) layers. This process of expansion can result in the detachment of active materials from conductive additives, accelerating the degradation of battery capacity. Furthermore, the uneven expansion of active materials due to lithiation disparities can generate localized stress and strain, eventually causing electrode cracking and detachment from the current collector [4].

To overcome such limitations, nano-structuring silicon particles into different sizes and morphologies such as silicon nanotubes [5], nanowires [6], nanodots [7] are found effective. By reducing the average size of the active material to the nanometer scale, the internal stress

* Corresponding author.

E-mail addresses: yangfan@sztu.edu.cn (F. Yang), liuqingxia@sztu.edu.cn (Q. Liu), tangzeguo@sztu.edu.cn (Z. Tang).

¹ These authors contributed equally.

generated during lithiation is significantly reduced at the same degree of lithiation [8]. Another strategy for enhancing the electrochemical performance of silicon-based anodes involves the incorporation or encapsulation of silicon nanoparticles within a carbon matrix [9–11]. This carbon matrix serves as a protective layer on the silicon surface, mitigating expansion-induced stress, preventing direct contact with the electrolyte and improving the material conductivity [12].

An ideal carbon matrix should be a continuous phase, completely enveloping the silicon surface. Such an arrangement ensures effective segregation of silicon nanoparticles and provides a stable foundation for the growth of SEI [12]. Typically, realization of such carbon coatings on silicon involves an initial coating with an organic carbon precursor, followed by a carbonization treatment [13–15]. However, due to its brittle nature, these carbon coatings tend to be fragile and can easily fracture when subjected to internal expansion forces [16]. Solving these challenges involves the design and synthesis of complex carbon-silicon hybrid structures, such as hollow [17,18], hierarchical arrangements [19,20], and yolk-shell configurations [21]. While these intricate Si-C composites can occasionally yield satisfactory outcomes, the high cost, tedious manufacturing process and use of hazardous materials such as strong acids in manufacturing process limit the production of these materials only at lab-scales, diminishing their commercial applications [22].

Besides such bottom-up approaches, alternative strategies involve incorporating silicon nanoparticles onto pre-existing stable carbon structures or phases, such as porous carbon [10], carbon nanotubes [23], and carbon fibers [24] that can serve as stable pathways for conductivity. However, traditional methods of mixing silicon particles with carbon materials rely on physical blending techniques [25,26]. This approach often struggles to achieve the necessary uniformity in composition due to issues such as uneven wetting and uncontrollable aggregation of silicon particles within the system. The weak bonding between silicon and the conductive network, along with inconsistencies in these carbon-silicon systems, contribute significantly to the rapid deterioration of conductive connections over extended charge/discharge cycles, thus hindering their widespread commercial adoption [27,28]. Consequently, there is a pressing need to develop a methodology capable of providing a robust coating layer and establishing a uniform and stable conductive network through scalable production methods. This is essential for practical applications of silicon as lithium-ion anode materials.

Among the various carbon-based materials under investigation, graphene attracts significant attention due to its outstanding mechanical strength, low linear expansion coefficient, chemical resistance, and electrical conductivity [29]. Nevertheless, the hydrophobic nature of graphene often leads to severe aggregation in most solvents, making it challenging to create a homogeneous slurry accommodating both silicon and graphene [30]. An alternative is graphene oxide (GO), a graphene derivative featuring oxygen functional groups that greatly enhance its dispersibility in solvents. When silicon and GO are combined in a compatible solvent, they can interact through molecular associations facilitated by hydroxyl or carboxyl groups [31]. Subsequent reduction of GO at elevated temperatures results in the formation of silicon-reduced GO (Si-rGO) composites. The electrochemical performance of Si-rGO composites as anodes hinges on the extent to which silicon nanoparticles are enveloped or encapsulated by rGO. Ideally, high-performance Si-rGO composites should meet several structural criteria: 1. Silicon nanoparticles should be extensively covered by rGO to minimize direct contact with the electrolyte. 2. The relative positions of silicon and rGO should remain stable even after multiple cycles of volumetric changes in silicon. This implies that silicon nanoparticles should ideally be anchored to rGO through a specific mechanism to prevent agglomeration of either silicon or rGO particles when external conditions change. 3. rGO should expand and maintain a flexible envelope around silicon nanoparticles when they undergo volumetric changes, providing ample protective shielding against undesirable

electrolyte reactions on silicon surfaces. 4. rGO should not readily fold or develop excessive wrinkles that could displace some of the silicon particles from its protective coverage.

In a traditional preparation method employing mixing GO and Si together followed by a thermal reduction treatment, these structural prerequisites are not easily met. This difficulty arises from the fact that, within the same thermal environment, silicon and GO typically undergo distinct surface property alterations. For instance, while silicon consistently maintains a hydrophilic nature during thermal reduction, GO undergoes a significant wettability transition from highly hydrophilic to highly hydrophobic (rGO). These discrepancies frequently lead to pronounced phase segregations between silicon and graphene. As a result, the coverage rate of rGO on silicon diminishes and substantial wrinkling of rGO occurs.

FJH technology is a thermal treatment method based on Joule heating principle. The whole thermal treatment process features exceptionally high heating/cooling rate of up to 10^5 K/s, with reaction temperatures reaching over 3000 K. This approach enables the synthesis of high-performance electrode materials within minutes [32,33]. It was found in this work that under specific FJH conditions, formation of silicon carbide at the interface between GO and silicon particles is obvious and can act as “riveting point” to effectively bond rGO and Si particles together. The initial discharge specific capacity of the prepared material reached $1141.3 \text{ mAh g}^{-1}$ at a current density of 1C (equivalent to 2280 mAh g^{-1} or 10.1 A/m^2), with a Coulombic efficiency exceeding 99 % from the second cycle onwards. Remarkably, even after 1000 charge-discharge cycles, the F-Si@rGO composite retained a specific capacity of $894.95 \text{ mAh g}^{-1}$, representing an average capacity degradation of only 0.0216 % per cycle. Extended cycling tests demonstrated competitive electrochemical performance and remarkable stability of the F-Si@rGO anode, with a remaining capacity of $651.67 \text{ mAh g}^{-1}$ after 2000 cycles. This synthetic approach not only holds promise for the development of graphene-based energy storage materials but also presents opportunities for broader applications in scenarios requiring graphene surface installation and processing.

2. Experimental procedures

2.1. Material preparation

A homogeneous GO aqueous solution was firstly prepared by diluting a GO solution (Shanxi Institute of Coal Chemistry, Chinese Academy of Sciences) with deionized water to a desired concentration of 4 mg ml^{-1} . Si powders (size $\approx 200 \text{ nm}$, Canrd New Energy Technology Co. Ltd.) were then homogenized into the GO dispersion by ball milling (equipment: MITR, YXQM-4I). A 100 ml ZrO_2 jar with ZrO_2 balls (size $\approx 3 \text{ mm}$) and a mass ratio of balls to slurry of 10:1 were used in the milling process, which was conducted at 300 rpm for 12 h to ensure a stable slurry containing Si-GO assemblies with a silicon content from 30 % to 70 % wt. To preserve the structural integrity of the already formed Si-GO assembly, the slurry containing Si-GO assemblies was subjected to rapid freezing by placing it in a -55°C cold trap for 12 h and subsequently freeze-dried under vacuum conditions of 0.01 Pa at -55°C for 24 h to remove the water content. After freeze-drying, the material underwent processing using an FJH processor (model HTS-7026D, Shenzhen Joule IC Technology Co., Ltd.), resulting in the production of the F-Si@rGO composite. Within the processor, the material was enveloped in a carbon wrap measuring 3 cm by 5 cm and positioned between two tungsten carbide electrodes spaced 4 cm apart in a gas-tight glass reaction chamber (size of $0.2 \text{ m} \times 0.3 \text{ m} \times 0.3 \text{ m}$). Processing conditions comprised a voltage of 50 V and a current of 20 A, maintained at 1000°C for 120 s with a heating rate of $1000^\circ\text{C s}^{-1}$. The rapid heating rate was found to be essential for achieving the desired microstructures. To highlight the advantageous effect of fast heating speed, a parallel heat treatment was conducted using the same material in a tube furnace with a significantly slower heat-up rate of 5°C min^{-1} (approximately 12,000

times slower compared to the FJH process). This slow heat treatment, lasting 120 s at 1000 °C, yielded the S-Si@rGO composite. Both heating processes were performed in an Argon environment with a flow rate of 1.5 L/min to prevent oxidation.

2.2. Material characterizations

The microscopic structures and surface morphologies of the prepared materials were characterized by Scanning Electron Microscopy (SEM, GeminiSEM 300, Carl Zeiss Microscopy Ltd., UK) coupled with Energy Dispersive X-Ray Spectrometry (EDS) and a Transmission Electron Microscopy (TEM, FEI Talos F200X).

X-Ray Diffraction (XRD, SmartLab XRD, Rigaku, Japan Inc.) was used to reveal the crystallinity of the samples. The incident radiation used in the XRD testing has a wavelength of 0.1542 nm (Cu K α). The testing is conducted with a voltage and current of 40 kV and 40 mA, respectively. The 2 θ interval is set to 24.225 s, with a step size of 0.0131303 degrees. The databases employed include PDF#99-0092 and PDF#99-00975.

X-Ray Photoelectron Spectroscopy (XPS, XPS Escalab Xi⁺, Thermo Fisher Scientific Co. Ltd, Czech) was used to analyze the changes in the functional groups and surface bonds. A micro-focused monochromatic Al target was used as the X-ray source, with a micro-focus spot size of 500 μ m, and all samples were calibrated with 284 eV (binding energy of sp² hybrid carbon) as C1s. The deconvolution of the spectra was performed by utilizing Gaussian functions within the XPS PEAK program, following the subtraction of a Shirley background.

2.3. Electrochemical characterizations

For the preparation of electrode materials, F-Si@rGO nanoparticles or S-Si@rGO nanoparticles were combined with conductive black (super P) and sodium carboxymethylcellulose (CMC) binder. The mass ratio employed was 8:1:1. These constituents were dispersed in a suitable amount of deionized water to create homogeneous slurries. Subsequently, these slurries were applied onto a Cu foil substrate and subjected to vacuum drying at 80 °C for a duration of 12 h, resulting in the formation of a uniform electrode layer.

To construct standard CR2032-type half cells, the assembly process was conducted in an Argon-filled glove box. Li metal foil was utilized as the counter electrode, while a polypropylene membrane as the separator. The electrolyte employed was 1 mol/L solution of LiPF₆ dissolved in a mixture comprising ethylene carbonate (EC), dimethyl carbonate (DMC), and ethyl methyl carbonate (EMC) with a volumetric ratio of 1:1:1, supplemented with 1 % wt. of vinylene carbonate (VC).

The silicon mass loading in the working electrodes was approximately 0.5 mg·cm⁻² for various electrochemical tests, including galvanostatic charging/discharging tests, galvanostatic intermittent titration measurements (GITT), cyclic voltammetry tests (CV) and electrochemical impedance spectroscopy (EIS). Furthermore, the same anode material was evaluated in an assembled full cell with the cathode being composed of LiFePO₄/super P/Polyvinylidene Fluoride (PVDF) at a mass ratio of 8:1:1 on aluminum foil. All electrochemical assessments were carried out at room temperature.

Galvanostatic charging/discharging tests were conducted on a Neware instrument (Shenzhen, China) over a voltage range of 0.01–1.5 V for half-cell and 2.5–3.5 V for full cell. CV and EIS measurements were conducted using a CHI 660e electrochemical workstation with a standard three-electrode setup. CV curves were generated by scanning voltage in the range of 0 to 3 V at a scan rate of 0.1 mV·s⁻¹, while EIS experiments were performed across a frequency range spanning from 0.01 Hz to 1 M Hz.

3. Results and discussion

3.1. Synthesis and material characterizations

As depicted in Fig. 1a, the synthesis process begins with the mixing of silicon nanoparticles and GO through ball milling. Notably, both silicon nanoparticles and GO sheets exhibit a substantial presence of oxygen-containing functional groups, which can lead to self-agglomeration when dispersed in water. Ball milling can allow sufficient breakup of the GO and silicon particle agglomerates and create enough collision opportunities for the silicon particles to be installed on the surface of GO sheets through interactions between oxygen-containing functional groups [34]. Sufficient time is allowed for the silicon nanoparticles to be anchored onto the GO sheets before the mixture undergoes freeze drying to eliminate water content. This step minimizes the risk of undesirable secondary self-agglomeration between silicon nanoparticles or GO sheets. Freeze drying is selected due to its scalability and industrial applicability, ensuring minimal disturbance to the established installations during water removal. The resulting material from freeze drying (Si@GO) exhibits a fluffy consistency and proceeds directly to the FJH treatment. During FJH, the material is compacted within a soft carbon fabric encasement positioned between two tungsten carbide electrodes. Subsequently, the material undergoes a programmed electrothermal processing in Argon as part of the FJH treatment to yield F-Si@rGO composite. For comparison, a traditional slow heat treatment in Argon was used to prepare S-Si@rGO composite from Si@GO.

Fig. 1b and c present the SEM characterizations of the Si@GO, S-Si@rGO and F-Si@rGO composites. In the case of Si@GO, silicon nanoparticles are evenly distributed on the GO surface (inset in Fig. 1b). However, upon subjecting Si@GO to a gradual thermal treatment, pronounced phase segregation becomes evident in the final product (S-Si@rGO). Within S-Si@rGO, rGO sheets display a wrinkled appearance and the silicon nanoparticles agglomerate, no longer maintaining coverage by the rGO sheets (Fig. 1b).

Despite the application of freeze-drying to mitigate structural disruption, the slow heating process promotes phase segregation by introducing varying degrees of wettability modification to the silicon and carbon phases. The silicon surface initially possesses hydroxyl groups that can interact with functional groups on GO via non-covalent bonds. As the GO sheets gradually lose their oxygen functional groups, the interaction between silicon and GO diminishes, leading to slow yet irreversible self-agglomeration among the silicon nanoparticles. Simultaneously, with the reduction of oxygen-containing functional groups, interactions within the π -systems of rGO become dominant, resulting in the folding of carbon sheets. This self-agglomeration contributes to the expulsion of hydrophilic silicon aggregates from the carbon matrix.

Severe phase segregation can be confirmed by dispersing a portion of the S-Si@rGO composite into a small container containing heptane (at the top) and water (at the bottom). Upon subjecting the container to 30 s of sonication, a partitioning phenomenon becomes apparent. Specifically, a black layer was formed at the top comprising hydrophobic agglomerates of rGO that migrate into the heptane phase, while a brown aqueous layer was at the bottom which is dominated by uniformly dispersed silicon nanoparticles (Fig. 1d). This phase separation is clearly visible through SEM (Fig. 1e and f). Notably, subjecting F-Si@rGO to the same partitioning tests (sonication in a container filled with heptane and water) demonstrates that such disturbance is insufficient to disengage the silicon nanoparticles from their anchoring points. Furthermore, F-Si@rGO exhibits surface activity and the capability to stabilize a water-in-heptane emulsion (Fig. 1g). This observation conclusively confirms the biwettability of F-Si@rGO particles, an attribute resulting from the coexistence of hydrophobic domains (rGO) and hydrophilic domains (silicon) within the same composite particle. SEM of F-Si@rGO in the binary mixture of heptane and deionized water also confirms this viewpoint (Fig. 1h).

Also, the morphology of F-Si@rGO shows that the rGO sheets be

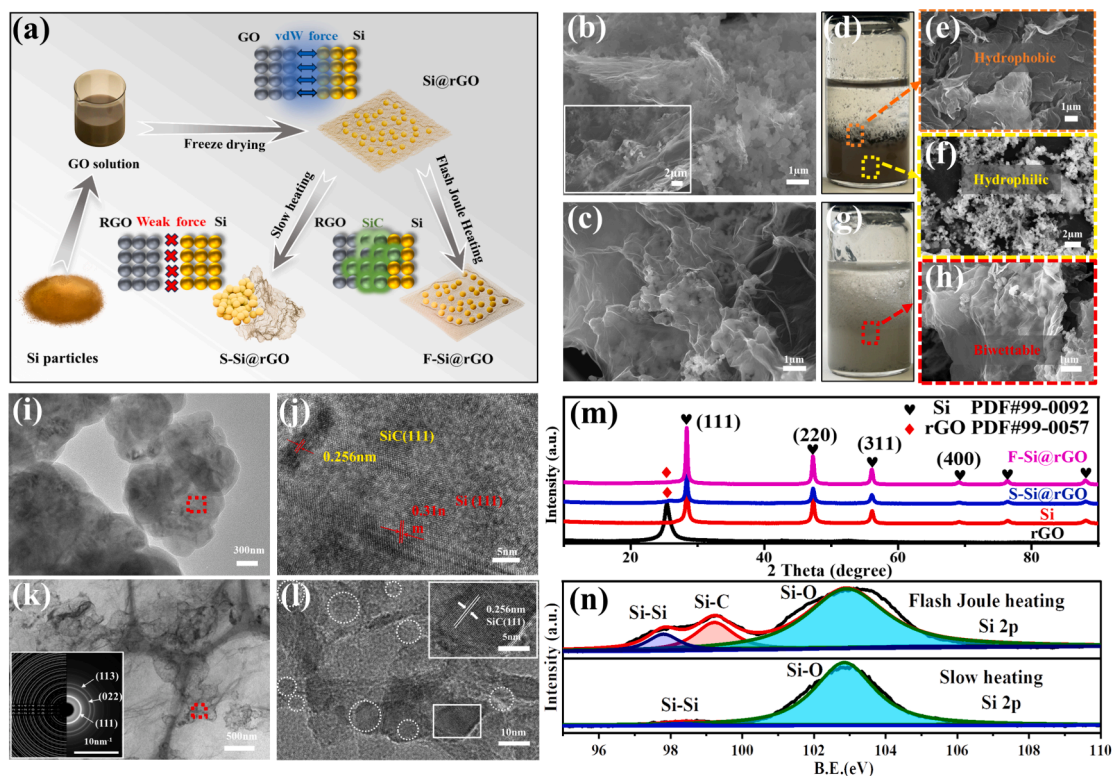


Fig. 1. Synthesis and material characterization of the prepared composites: a) Schematic of the synthesis routes of F-Si@rGO and S-Si@rGO composites. b) SEM image of S-Si@rGO, inset shows micro-morphology of Si@GO. c) SEM image of F-Si@rGO. d) Partitioning behavior of S-Si@rGO in the binary mixture of heptane and deionized water. e) SEM image of S-Si@rGO at the interface between heptane and deionized water. f) SEM image of S-Si@rGO in the deionized water. g) Partitioning behavior of F-Si@rGO in the binary mixture of heptane and deionized water. h) SEM image of F-Si@rGO in the binary mixture of heptane and deionized water. i) and j) HRTEM image of F-Si@rGO. k) and l) HRTEM image of F-Si@rGO in which silicon has been dissolved by sodium hydroxide solution (the inset shows SAED pattern). m) XRD patterns of F-Si@rGO, S-Si@rGO, Si and rGO. n) The XPS spectrum (Si 2p) of the two prepared composites.

more expanded and thinner, with the silicon nanoparticles appeared in smaller domains of agglomerates which are completely wrapped by rGO. The drastic morphological difference between S-Si@rGO and F-Si@rGO is likely dependent on how fast the system can react to surface property change. FJH treatment induces a significant temperature increase within milliseconds, thereby affording minimal reaction time for silicon nanoparticles to migrate within the GO matrix during the electrothermal treatment. Sufficient contacts between silicon and rGO encourages the formation of anchoring points between silicon and rGO, thereby ensuring the relative positioning of silicon nanoparticles within the carbon matrix. These anchoring points are discernible in HRTEM micrographs as diminutive shaded regions (Fig. 1i and j), featuring a d-spacing of approximately 0.256 nm, corresponding to the (111) plane of the SiC crystalline structure [35]. The robustness of these anchoring points arises from the formation of covalent bonds between silicon and carbon.

To obtain a clearer perspective on the positioning and distribution of SiC anchoring points within the rGO matrix, the silicon phase in the F-Si@rGO composite was selectively removed using a 1 mol/L sodium hydroxide solution. In Fig. 1k and l, it is evident that, following the removal of the silicon phase, rGO "bubbles" become apparent, signifying the encapsulation of the silicon phase by carbon in the original structure. On the surface of these rGO "bubbles", an abundance of dispersed single crystals was observed, resilient to removal by strong base. The Selected Area Electron Diffraction (SAED) test indicates three distinct diffraction rings corresponding to the (113), (022), and (113) crystal planes in silicon carbide crystals according to COD 1010995 from the Crystallography Open Database (inset in Fig. 1k). This finding complements the HRTEM micrographs on the chemical nature of these anchor points.

The crystalline phase and structure of the composites were further

analyzed by XRD. In Fig. 1m, the signature diffraction peaks of silicon (28.44° , 47.30° , 56.12° , 69.13° , 76.37° and 88.03°) and rGO (25.88°) can be easily found. The rGO peak in the XRD pattern of the S-Si@rGO composite is significantly stronger than that of the F-Si@rGO composite, consistent with the observation in SEM micrographs that the rGO sheets are more agglomerated in the S-Si@rGO composite. Fig. S1 shows the comprehensive XPS spectrum of the composite anode material. Magnification of the Si 2p spectrum (Fig. 1n) for the S-Si@rGO composite displays two distinct peaks at 98.41 eV and 102.86 eV, corresponding to Si-Si and Si-O bonds, respectively. Notably, the Si 2p spectrum of F-Si@rGO exhibits an additional peak at 99.2 eV, indicative of the presence of a Si-C bond, providing additional evidence for the formation of silicon carbide within the F-Si@rGO composite. Be noted that in nano-crystalline silicon, the surface layers can exhibit some degree of amorphous character due to the high surface-to-volume ratio and the presence of defects [36]. This amorphous layer on the surface of nano-crystalline silicon enhances its reactivity, providing ample opportunities for chemical reactions with graphene at elevated temperatures. The disordered structure of amorphous silicon leads to increased surface energy and facilitates the diffusion of carbon atoms from graphene into the silicon lattice and thus can promote the formation of SiC at the graphene-silicon interface.

3.2. Electrochemical performance of F-Si@rGO and S-Si@rGO electrodes

Cyclic voltammetry (CV) analysis at a scan rate of 0.1 mV s^{-1} between 0 and 3 V (vs. Li/Li^+) were conducted to illustrate the activation process of F-Si@rGO and S-Si@rGO in the initial five cycles. For F-Si@rGO (Fig. 2a), an insignificant reduction peak appeared in the initial cathodic scan at around 0.71 V, corresponding to the formation of SEI

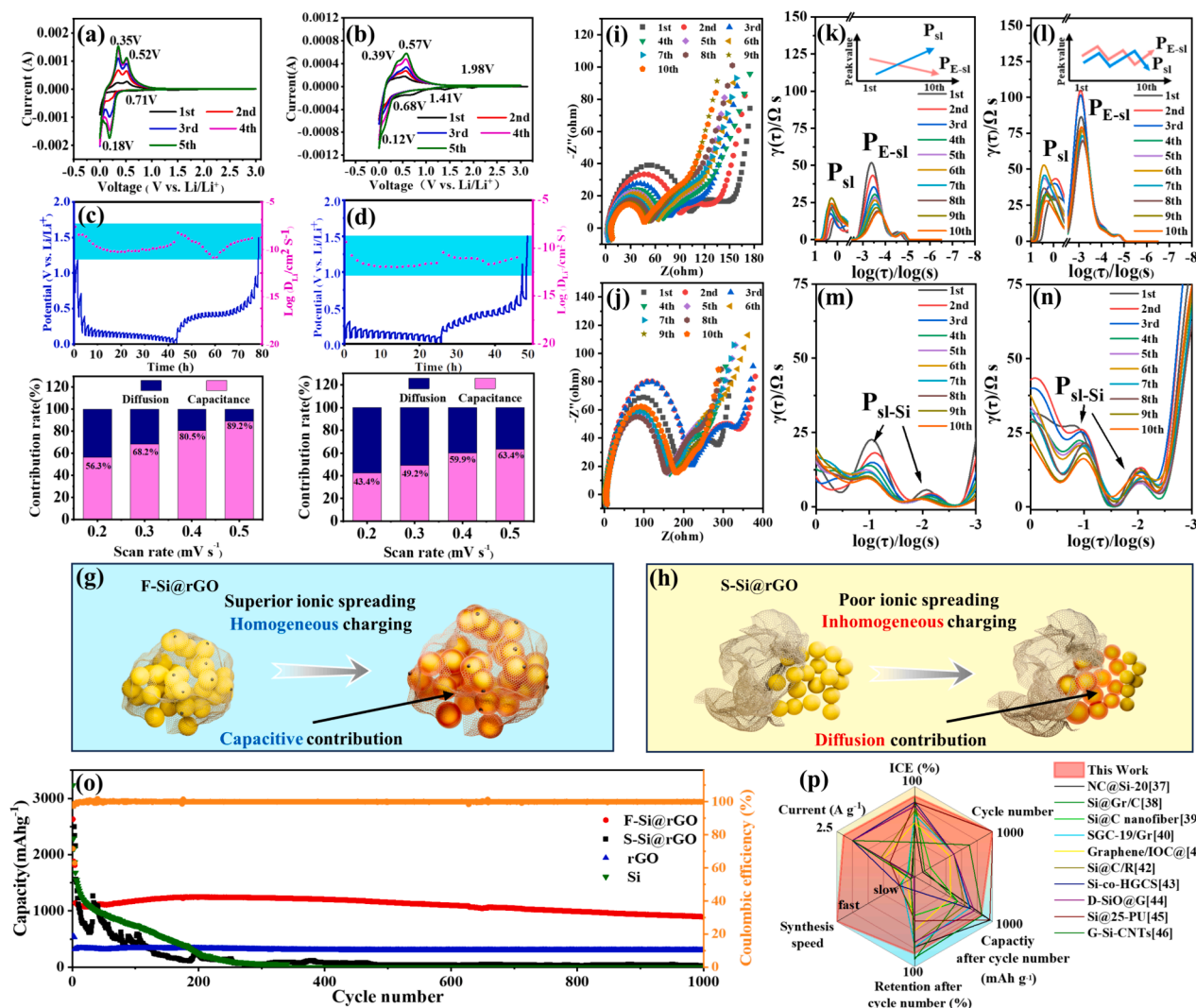


Fig. 2. Electrochemical performance of the prepared composites: a) CV curves of the F-Si@rGO electrode. b) CV curves of the S-Si@rGO electrode. c) GITT curves of F-Si@rGO. d) GITT curves of S-Si@rGO. e) Capacitive contribution ratio of F-Si@rGO at different scan rates. f) Capacitive contribution ratio of S-Si@rGO at different scan rates. g) Schematic representation of capacitive dominated charging process in F-Si@rGO. h) Schematic representation of diffusion dominated charging process in S-Si@rGO. i) EIS curves of F-Si@rGO. j) EIS curves of S-Si@rGO. k) DRT function plots $\gamma(\tau)$ of F-Si@rGO between 1–10 s and below 10^{-3} s. l) DRT function plots $\gamma(\tau)$ of S-Si@rGO between 1–10 s and below 10^{-3} s. m) DRT function plots $\gamma(\tau)$ of F-Si@rGO between 1– 10^{-3} s. n) DRT function plots $\gamma(\tau)$ of S-Si@rGO between 1– 10^{-3} s. o) Long-term cycling performances of the prepared composites at 1C. p) Comparison of performance of F-Si@rGO with previous reported Si-based materials [37–46].

layer. Such a reduction peak disappeared in the following cycles, suggesting that SEI layer formed and stabilized in the first cycle discourages further SEI growth. In comparison, three reduction peaks located at 1.98 V, 1.41 V and 0.68 V are prominent for S-Si@rGO, suggesting that SEI growth happened on different interfaces and was much more severe in the case of S-Si@rGO (Fig. 2b).

This observation is consistent with the severe phase segregation observed in the microscopic morphology of S-Si@rGO, that electrolyte consumption and thus SEI growth can happen at various exposed surfaces of S-Si@rGO to electrolyte. Furthermore, the anodic peaks at 0.18 V for F-Si@rGO and 0.12 V for S-Si@rGO are attributed to the reduction of Si to Li_xSi phases, while the cathodic peaks for F-Si@rGO (at 0.35 V and 0.52 V) and S-Si@rGO (at 0.39 V and 0.57 V) are related to the phase transformation of Li_xSi to amorphous Si [47]. The potential gap between the anodic and cathodic peaks (ΔE_p) signifies the level of energy required for Li⁺ to migrate in or out of the anode materials, and the speed of the electrochemical reaction. Thus, a smaller ΔE_p of F-Si@rGO compared S-Si@rGO (0.17 V vs. 0.27 V) suggests F-Si@rGO bears higher ionic conductivity and electrochemical activity. Higher ionic

conductivity ensures F-Si@rGO displays a high initial capacity of 2383.7 mAh g⁻¹ and an impressive initial Coulombic efficiency (ICE) of 88.7 % at a current density of 0.05 C (Fig. S2).

The Li⁺ diffusion coefficient (D_{Li}^+) was determined using the Galvanostatic Intermittent Titration Technique (GITT). As presented in Fig. 2c and d, D_{Li}^+ of the F-Si@rGO electrode is always one to two orders of magnitude higher than that of S-Si@rGO electrode. The enhanced Li⁺ diffusion kinetics observed in the F-Si@rGO electrode can be attributed to the presence of silicon carbide anchors, which promote closer contact between silicon and graphene. This establishment of stronger and more efficient pathways for lithium-ion diffusion is the key factor behind the observed enhancement.

From a kinetic perspective, measuring the response current (i) of electrode materials at various scan rates (v) is widely considered the most suitable method for identifying electrochemical processes based on battery-type (diffusion-controlled) or capacitive (surface-controlled) charge storage. To gain insight into the mechanisms governing the electrochemical performance, cyclic voltammetry (CV) curves of F-Si@rGO and S-Si@rGO are registered at different scan rates, ranging

from 0.1 to 0.5 mV s^{-1} (Fig. S3a). By applying the power law, the slope of the plot $\log(i)$ vs. $\log(v)$ (redox peak current vs. various scan rates) yields the b -value which serves as an indicator of the predominant mechanism governing the energy storage behavior of the active materials [48]. Specifically, a b -value of 0.5 suggests a diffusion-controlled redox reaction, primarily involving intercalation/conversion/alloying reactions and b -value of 1.0 indicates a surface-limited electrochemical process, such as a pseudocapacitive storage process [48,49]. The calculated b -values for the oxidation and reduction peaks of F-Si@rGO are 0.97 and 0.935 respectively (Fig. S3b, calculation process detailed in Supporting information), suggesting that the lithiation and delithiation cycles in F-Si@rGO are primarily driven by a capacitive process. Furthermore, the contribution of capacitance to the overall capacity (as shown in Fig. 2e) increases with higher scan rates, eventually reaching a proportion of 89.2 % at a scan rate of 0.5 mV s^{-1} (Calculation processes for capacitive ratios of F-Si@rGO and S-Si@rGO are shown in Figs. S4 and S5 respectively). This underscores the remarkable rate performance of F-Si@rGO, which can be attributed to its capacitive behavior.

Conversely, the b -values of S-Si@rGO for the oxidation and reduction peaks of S-Si@rGO are 0.615 and 0.494 (shown in Fig. S6a and b), which indicates the S-Si@rGO exhibits a diffusion-dominated charging process. The capacitance contribution to the capacity is 43.4 % and 63.4 % at scan rates of 0.2 mV s^{-1} and 0.5 mV s^{-1} (shown in Fig. 2f) respectively. These values are notably lower than the capacitance contribution of 56.3 % and 89.2 % observed in F-Si@rGO when operating at the same scan rates.

To understand the differences in the ratios of capacitance contributions, schematics of the possible storage mechanisms in F-Si@rGO and S-Si@rGO were shown in Fig. 2g and h respectively. The robust anchoring of silicon nanoparticles within a graphene matrix provides an extensive and uniformly distributed surface area for contact between silicon and carbon in F-Si@rGO. The carbon matrix functions as an ionic-conductive “highway,” facilitating the homogeneous transport of electrons and ions to the surface of silicon. This promotes superior ionic spreading on the silicon surface, contributing to energy storage through rapid and reversible redox reactions at the surface and subsurface of the silicon nanoparticles. On the other hand, when such continuous conductive-pathways are lacking, as in the case of S-Si@rGO, charge transport may rely more on diffusive processes within the bulk of the active material. The exchange of Li^+ and electrons through solid state diffusion can allow for a degree of electric connectivity within the material but is inefficient and may eventually lead to inhomogeneous charging that silicon nanoparticles in contact with the rGO will experience more efficient charge transfer compared to silicon particles that are not in direct contact with the conductive matrix.

Electrochemical Impedance Spectroscopy (EIS) is used to analyze the impedance of the electrode materials. Both Nyquist plots in Fig. 2i (F-Si@rGO) and j (S-Si@rGO) display two semicircles in the high and medium frequency ranges and an inclined straight line in the low frequency range. The distinct semicircle within the high frequency region is associated to the interface resistance between the electrolyte and SEI on the electrode. The semicircle in the medium frequency range corresponds to the charge transfer process at the interface between the surface layer and the silicon and the inclined straight lines in the low frequency range corresponds to the diffusion-controlled impedance within the silicon phase [47]. For better clarity to see the change in the charge transfer resistance of the SEI, Nyquist plots of the 1st, 5th and 10th cycle of F-Si@rGO and S-Si@rGO respectively are plotted in Fig. S7. For both of F-Si@rGO and S-Si@rGO, the initial cycle exhibits a more pronounced charge transfer resistance with its magnitude decreasing as the cycling progresses. This trend suggests a densification of the SEI layer over cycling, thereby enhancing its charge transfer capabilities. The Distribution of Relaxation Times analysis (DRT) conceptualizes an electrochemical system as a combination of an ohmic resistance and an infinite series of polarization processes. This methodology offers a reliable approximation to the impedance model of

electrochemical system, delivering insightful kinetic information regarding the anodic electrochemical reactions [50]. Assisted by the DRT tools pioneered by Ciucci's team [51], the peaks observed in the DRT function plots of S-Si@rGO (Fig. S8a) and F-Si@rGO (Fig. S8b) can be categorized into different electrochemical processes within the electrode based on the value of $\gamma(\tau)$: the signals upon 1 s (frequency below $1/2\pi$ Hz) are associated with the diffusion processes of solid, in which the peaks located at 1–10 s and >10 s represent the region division dictated by the Li-ion diffusion in the surface layer (P_{sl}) and silicon bulk (P_{sl}) respectively [52,53][60]. Signals located at higher frequencies usually indicates interfacial charge transfers. The peak ($P_{\text{sl-si}}$) located between 1 s and 10^{-3} s (medium frequency) are associated with the charge transfer resistance occurring between the surface layer and the Si bulk, and Peak ($P_{\text{E-si}}$) in $\gamma(\tau)$ below 10^{-3} s is attributed to the interfacial reaction process between electrolyte and the surface layer [54].

As shown in Fig. 2k and l, F-Si@rGO exhibits a lower magnitude of $P_{\text{E-si}}$ compared with S-Si@rGO. The value of the $P_{\text{E-si}}$ in F-Si@rGO becomes progressively smaller with cycling (inset in Fig. 2k). Be noted that the SEI layer start with a porous solid phase with the pores filled with electrolyte [55]. Therefore, in the initial cycles, the magnitude of $P_{\text{E-si}}$ which is attributed to the interfacial reaction between electrolyte and the surface layer predominantly contributes to the total impedance, primarily due to the extensive surface area contacts between SEI and electrolyte. The other part of the contribution arises from the diffusive processes within the surface layer (P_{sl}). Lower starting magnitude of $P_{\text{E-si}}$ with F-Si@rGO and the magnitude decreases along with cycling suggests the starting density of the SEI layer on F-Si@rGO is higher compared with S-Si@rGO and the interface between the SEI on F-Si@rGO and the electrolyte becomes increasingly conducive for charge transfer. Be noted that the exceptionally rapid heating capability of FJH ensures that the composite material remains at elevated temperatures for only a brief period, thereby mitigating the risk of crystallization, which can occur if high temperature exposure is prolonged. Unlike amorphous silicon, which undergoes direct lithiation [56], crystalline silicon must first undergo amorphization before full lithiation can occur. In the case of crystalline Si, lithiation predominantly progresses in the $\langle 110 \rangle$ direction, leading to additional isotropic stress that may adversely affect early SEI growth [57]. This likely accounts for the observed higher initial density of SEI with F-Si@rGO. In the case of F-Si@rGO, the gradual reduction of $P_{\text{E-si}}$ is accompanied by a mild increase in P_{sl} , indicating a transition from a liquid-phase reaction between the electrolyte and SEI to a solid-state reaction over multiple cycles. This solid-state evolution of the SEI enhances the cycling process by providing the required robustness to maintain the integrity of the SEI in the face of volumetric changes in the active materials.

In contrast, the initial value of $P_{\text{E-si}}$ in S-Si@rGO is notably higher, indicating that the SEI formed in this case possesses a lower initial density and lacks the robustness observed in F-Si@rGO. Both $P_{\text{E-si}}$ and P_{sl} in S-Si@rGO exhibit irregular, abrupt increases followed by subsequent decreases during the second, sixth, and eighth cycles (inset in Fig. 2l). This recurring fluctuation in impedance can be attributed to the significant expansion resulting from silicon lithiation. In scenarios where the SEI formation is less than ideal, such as when it has low mechanical strength or forms directly on the silicon surface, the repetitive volumetric changes in the active material lead to the continuous destruction and reformation of the SEI layers. This, in turn, consumes excessive amounts of electrolytes and results in the formation of unfavorable “dead zones” within the active materials.

Peaks of $\gamma(\tau)$ located between 1 s and 10^{-3} s (medium frequency) are dependent on the electrical contact between silicon and the conductive framework and surface layer. As shown in the Fig. 2m (F-Si@rGO) and n (S-Si@rGO), F-Si@rGO exhibits a much lower magnitude of $P_{\text{sl-si}}$ and both samples exhibit a similar trend as $P_{\text{E-si}}$, indicating that the presence of SiC anchors provides more contact points between Si and the carbon conductive framework, significantly enhancing the efficiency of lithium-ion diffusion.

Fig. 2o illustrates the long-cycle performance of F-Si@rGO, S-Si@rGO, Si particles and rGO. All test batteries underwent activation with a low current density of 0.05C for the first five cycles before they were tested at a current density of 1C. F-Si@rGO exhibited a high initial capacity of 1141.3 mAh g⁻¹ at a current density of 1C, and demonstrated superior retention compared with S-Si@rGO and Si. Remarkably, after 1000 cycles, the capacity of F-Si@rGO remained at 894.95 mAh g⁻¹, corresponding to a capacity retention of 78.41 % in 1000 cycles. Furthermore, even after enduring an astonishing 2500 charge–discharge cycles, F-Si@rGO maintained an impressive capacity of 574.47 mAh g⁻¹ (see Fig. S9). The rate performance of F-Si@rGO, presented in Fig. S10, demonstrated excellent performance across a range of current densities (0.1C to 1C).

Compared to previous research on silicon-carbon composite materials (Fig. 2p and Chart S1), F-Si@rGO prepared via FJH demonstrates superior electrochemical performance across various metrics including ICE, cycle number tested, current density, capacity retention and post-cycling capacity. Additionally, its fast synthesis speed positions it as a viable candidate for industrial-scale production, offering promising potentials for commercialization.

3.3. Mechanism of the improved performance of F-Si@rGO

To assess the growth of SEI and integrity evolution of these two different electrodes, the cycled batteries (after 500 cycles) were placed in a glovebox where their shells were opened by pliers and the electrodes within were extracted with care. The electrodes were then soaked and cleaned with anhydrous ethanol to remove the remaining electrolyte before being dried at room temperature in Argon to have their morphology examined. The structures of the active materials within the electrodes were examined by transmission electron microscopy (TEM) imaging and energy-dispersive X-ray spectroscopy (EDS) for elemental mapping. As illustrated in Fig. 3a, S-Si@rGO exhibited severe pulverization of silicon particles after 500 cycles. The original spherical shape of silicon was completely lost, transforming the composite into a mixture characterized by a relatively homogeneous distribution of silicon, carbon (C), and fluorine (F) atoms (indicative of SEI growth) (Fig. 3b, c and d). In contrast, F-Si@rGO maintained its structural integrity, with the spherical shape of silicon clearly discernible after 500 cycles (see Fig. 3e). Notably, EDS mapping of the F-Si@rGO composite revealed that carbon and fluorine elements were predominantly concentrated at the periphery of silicon particles (as seen in Fig. 3f, g and h). This suggests that SEI growth primarily occurred on the outer layer of rGO, where unnecessary side-reactions were effectively prevented and thus

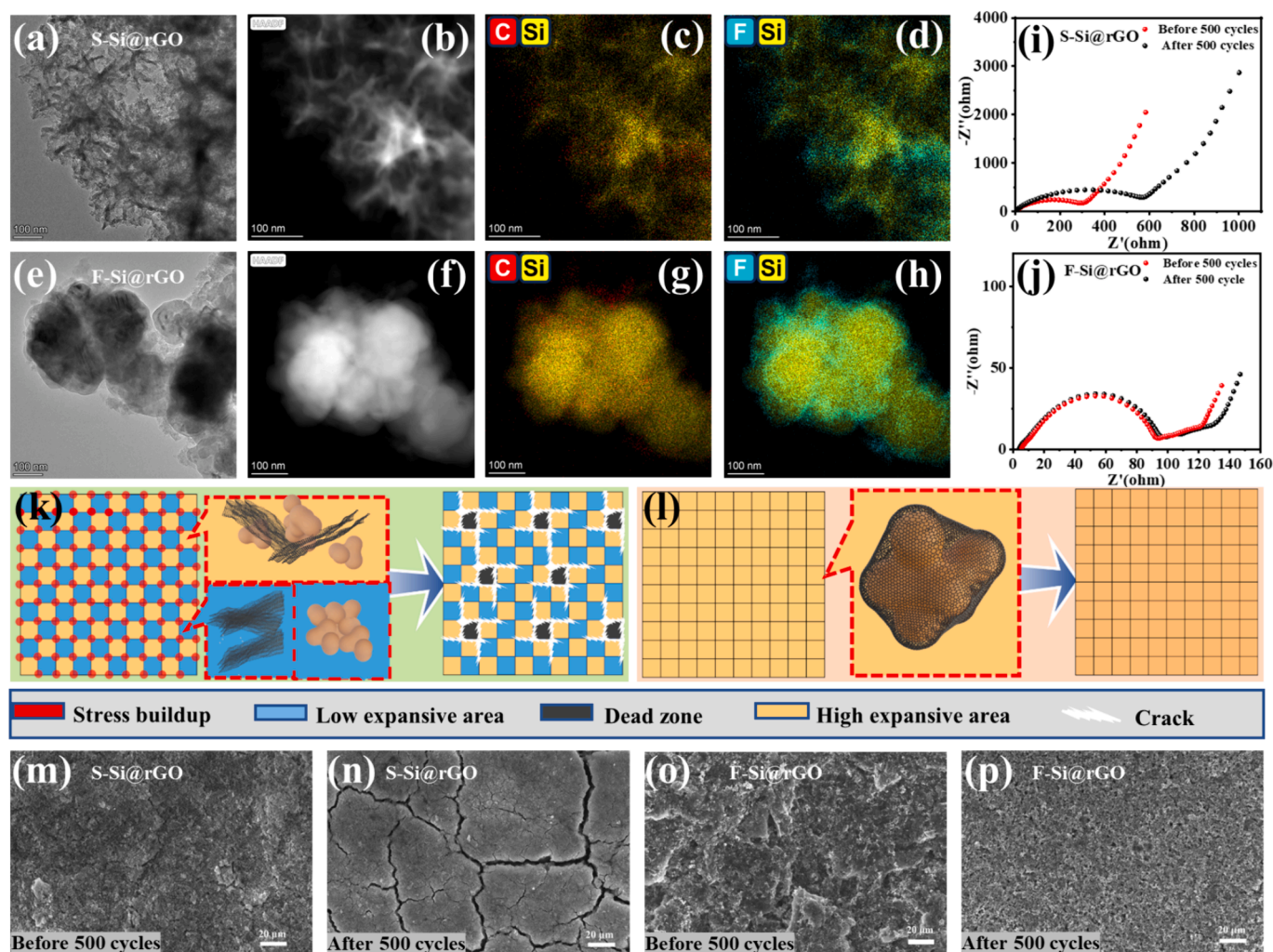


Fig. 3. a) HRTEM image of S-Si@rGO after 500 cycles. b), c) and d) EDS element mapping of S-Si@rGO after 500 cycles. e) HRTEM image of F-Si@rGO after 500 cycles. f), g) and h) EDS element mapping of F-Si@rGO after 500 cycles. i) EIS curves of S-Si@rGO after cycles. j) EIS curves of F-Si@rGO after cycles. k) Microscopic schematic of the cycling process of S-Si@rGO. l) Microscopic schematic of the cycling process of F-Si@rGO. m) The SEM images of S-Si@rGO before 500 cycles. n) The SEM images of S-Si@rGO after 500 cycles. o) The SEM images of F-Si@rGO before 500 cycles. p) The SEM images of F-Si@rGO after 500 cycles.

excessive SEI growth as seen in the case of S-Si@rGO avoided. On a microscopic scale, the process of lithiation in silicon is featured by the atomic ledge peeling mechanism that entails the gradual removal of atomic layers from the silicon surface by lithium ions, resulting in the formation of successive layers of an amorphous Li_xSi alloy [57]. As a consequence, the silicon anode experiences non-uniform expansion during lithiation. Within individual silicon nanoparticles, the anchored carbon matrix in F-Si@rGO promotes more uniform lithiation and homogeneous mobility of the interface between the lithiated amorphous Li_xSi and unlithiated Si core during charging and thus discourage the formation of fractures due to anisotropic swelling in silicon particles after long-term cycling. In S-Si@rGO, on the other hand, charge transport may rely more on lithium diffusion within the silicon bulk, that is, without satisfactory ionic spreading, the average pathway for lithium ions to reach full lithiation of silicon will be significantly longer, leading to uneven lithiation and consequently more fractures and severer SEI growth.

This substantial difference in morphology is also reflected in the change of resistance of these two materials. After 500 cycles, the resistance of S-Si@rGO increased by more than two-folds (refer to Fig. 3i) due to the extensive growth of SEI, severe phase segregation and silicon pulverization during prolonged cycling. In contrast, the resistance of F-Si@rGO remained largely unchanged due to the sustained integrity of the composite structure and the ideal SEI growth conditions (as shown in Fig. 3j). Be noted that the formation of the SEI layer commences during the activation process of the electrodes. This activation involves several initial cycles at a low rate (0.05 C), conducted before cycling the electrodes at high rate of 1C for 500 cycles. The absence of a semicircle in the medium-frequency range of the Nyquist plots, as observed in Fig. 3i and j after the activation process, suggests that the densification stage of the initially formed SEI layer is nearly completed within the initial activation cycles.

Significant cracks were also observed in the case of S-Si@rGO across the surface of electrode. This is likely due to the severe phase separations between rGO and silicon that leads to non-uniform charging of silicon particles across the electrode. During the electrode's operation, this non-uniform charging state introduces varying degrees of volumetric expansion within the electrode. Regions containing silicon nanoparticles enveloped by rGO experience higher levels of expansion, while areas with concentrated rGO or silicon show less volumetric expansion, due to the limited expansion characteristics of carbon or lack of conductivity in silicon.

As illustrated in Fig. 3k, the surface of the S-Si@rGO electrode is schematically represented as a checkered patterned box. In this representation, boxes in light yellow depict areas containing effectively charged silicon nanoparticles, while boxes in light blue indicate regions with severe phase segregations. The non-uniform volumetric changes caused by the distinct charging states can result in the development of significant localized stress concentrations (highlighted in red in Fig. 3k). These stress concentrations serve as initiation points for the formation of microcracks. The propagation and combination of these microcracks further compromise the conductivity within the electrode, leading to the creation of large "dead zones" where the active material completely loses its conductivity from other areas. On the other hand, F-Si@rGO exhibits a homogeneous charging state throughout different locations within the electrode, primarily due to minimized phase segregation and interfacial sintering (Fig. 3l). This results in significantly improved ionic wetting during the charging process and ultimately leads to a more uniform volumetric change throughout the electrode. As a result, it alleviates the development of micro-stress concentrations.

As a result, SEM imagery confirmed formation of numerous large cracks in the electrode of S-Si@rGO (Fig. 3m and n) after 500 cycles. Regional isolation in the electrode discourages electron and ionic transportation within the electrode and is one of the direct reasons for drastic impedance increase with cycling. In contrast, the surface of F-Si@rGO electrode (Fig. 3o and p) remains remarkably smooth without any

visible cracks after 500 cycles. This observation is consistent with the intact integrity of the composite structure in HRTEM after cycling.

3.4. Bench scale production and validation in $\text{LiFePO}_4/\text{F-Si@rGO}$ Full-Cells

The scalability of this synthesis method for F-Si@rGO particles is exemplified through a bench-scale demonstration, where it successfully treated 1 g of particles sandwiched between two $5\text{ cm} \times 5\text{ cm}$ carbon fabric layers (Fig. 4a). This setup utilized tungsten carbide electrodes to apply a high electric current to rapidly heat up the materials to 1000°C in $\sim 1\text{ s}$, with a total treatment duration of 100 s to produce F-Si@rGO. Notably, a total of just three runs, cumulatively lasting for only 5 min, produced sufficient F-Si@rGO to nearly fill a 100 ml glass beaker with $\sim 70\text{ ml}$ of material (Fig. 4b). It's important to note that this bench-scale process is primarily constrained by the carbon fabric's dimensions. Envisioning in an industrial-scale production, significantly larger carbon fabrics can be utilized. For instance, employing a $1.5\text{ m} \times 1.5\text{ m}$ carbon fabric could enhance the production rate by up to 900 times. This scale-up translates to an impressive output of 388.8 kg/day , assuming a 12-hour production cycle.

The F-Si@rGO particles produced in this bench-scale test underwent SEM characterization, verifying their morphological consistency with those produced in smaller batches (20 mg). As shown in Fig. 4c, the SEM images demonstrate that the bench-scale produced particles retain the key morphological features seen in smaller batch samples, with silicon nanoparticles effectively covered by thin layers of rGO. This consistency in structure suggests that the enhanced performance characteristics observed at a smaller scale may be replicable in larger productions. Furthermore, partitioning tests conducted on the bench-scale produced F-Si@rGO particles echoed the emulsion stabilization phenomenon seen in smaller-scale experiments (Fig. 4d). This consistency is encouraging and suggests a robust silicon-carbon integration in the F-Si@rGO composites, regardless of the batch size. These findings offer evidence of the scalability of this synthesis method and provide a foundation for future work aimed at adapting and validating the process for industrial applications.

As shown in Fig. 4e and f, a $\text{LiFePO}_4/\text{F-Si@rGO}$ full cell was constructed to test the practical application value of F-Si@rGO. The results of the cycle test performed at 1C show that the battery demonstrates satisfactory stability and remains a specific capacity of 120 mAh g^{-1} after 200 cycles. The rate performance of the as-prepared full cell was also evaluated by testing it at varying charging current densities, and satisfactory results were demonstrated, as illustrated in Fig. S13.

Industrialization of such nanocomposites requires exceptional scalability of the proposed synthesis route. Different from most of the other synthetic methods for complex silicon-carbon composites that involves high cost, tedious manufacturing process and use of hazardous materials such as strong acids, the proposed synthesis method here is simple, low cost and has great scale-up potentials.

Fig. 4g illustrates an envisioned production line for mass-producing F-Si@rGO integrating freeze-drying and FJH treatment. Freeze-drying is already a proven industrially viable dehydration method to preserve pharmaceuticals, biologicals, foods, and other heat-sensitive materials. FJH is currently employed in massive production of "flash" graphene and is expected to reach a production scale of 1 metric ton/day [58]. Freeze-dried Si@GO particles are fed into the FJH chamber via a carbon fiber weave roller belt. Two movable graphite electrodes compress the particles to achieve desired compactness and resistivity. During electrothermal operation, energy is concentrated on the reactants due to their highest resistivity, following Joule's law. Each batch's operation time can be as short as 100 s, and the F-Si@rGO product can be recovered using a rolling splitter that separates the upper and lower carbon fiber weaves. The simplicity, cost-effectiveness, and scalability of the proposed synthesis method present a promising solution to longstanding challenges associated with the production of silicon-carbon composites.

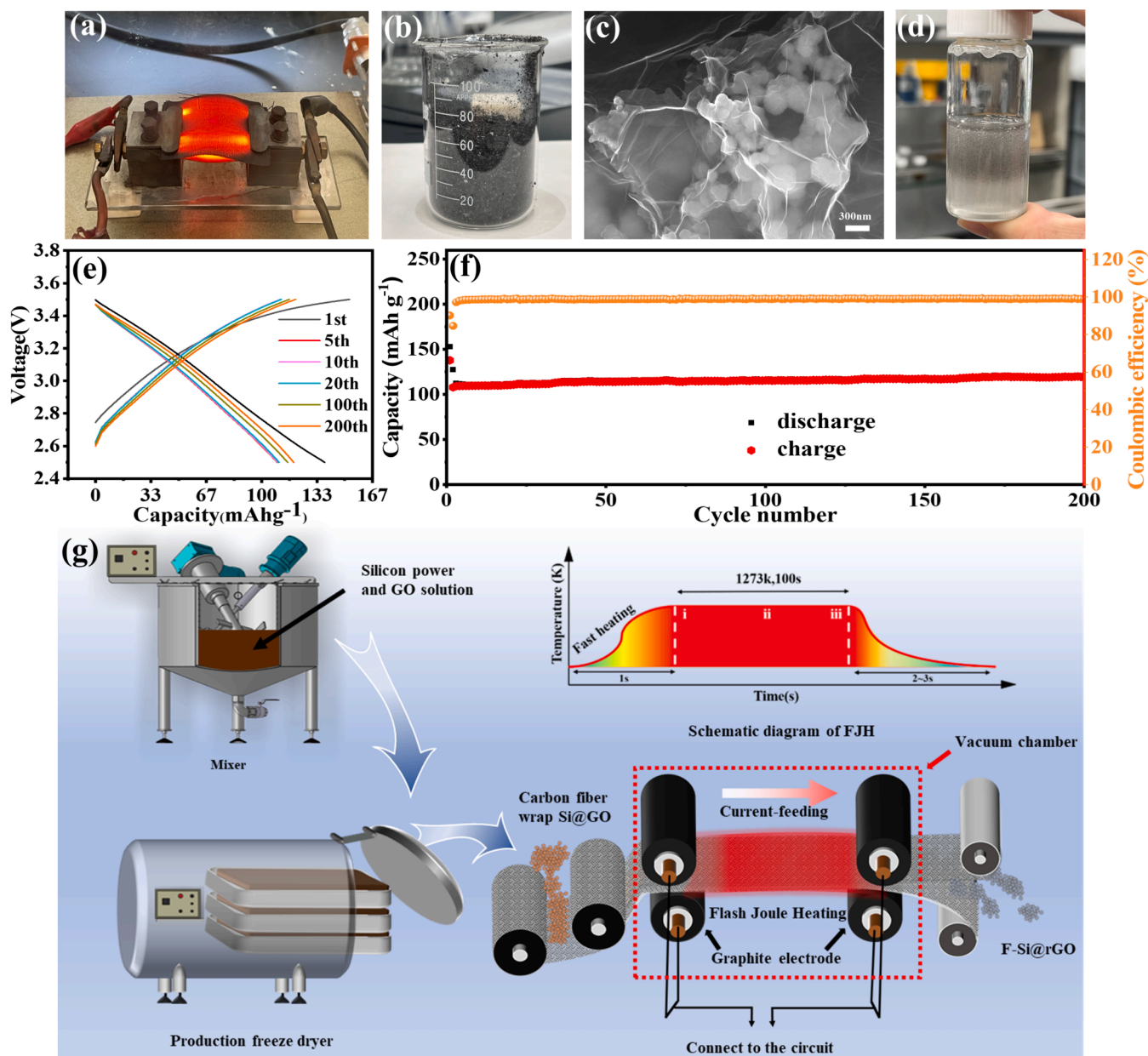


Fig. 4. Bench scale production of F-Si@rGO and its electrochemical performance in full cell tests: a) Bench scale production of F-Si@rGO in the laboratory. b) A jar of F-Si@rGO composites prepared within a total treatment time of 5 min. c) SEM of the prepared F-Si@rGO in the bench scale production. d) Partitioning behavior of the prepared F-Si@rGO in the binary mixture of heptane and deionized water. e) Voltage profiles of the full cell using F-Si@rGO as the anode and LiFePO₄ as the cathode; f) Long-term cyclability of the LiFePO₄/F-Si@rGO full cell at 1 C. g) Schematic illustration of scalable production of F-Si@rGO.

4. Conclusions

In this work, a simple, fast and scalable synthesis method for high performance silicon anodes of lithium-ion batteries is demonstrated. By rapidly welding Si and graphene together through an ultra-fast heating method based on Joule principle, it was demonstrated phase segregation between silicon nanoparticles and the graphene matrix during a conventional heat treatment was prevented. By introducing localized high temperature, a third phase of silicon carbide was formed between graphene and silicon which can serve as “riveting points” to securely anchor the silicon nanoparticles within the graphene matrix, even as repetitive volumetric changes occur during charge and discharge cycles. The robust graphene coverage on silicon also serves as a solid foundation for the controlled growth of SEI, effectively preventing undesirable secondary reactions between the electrolyte and the silicon surface. The

synthesized F-Si@rGO composite, as demonstrated in this study, exhibits an impressive capacity of 1141.3 mAh g⁻¹ at 1C and maintains a remarkable reversible capacity of 894.95 mAh g⁻¹ even after 1000 charge–discharge cycles, with an average capacity degradation of only 0.0216 % per cycle. This level of performance and durability is a significant step forward in the development of advanced graphene-based energy storage materials. The proposed synthesis method offers key advantages, including speed, controllability, and scalability, making it a promising avenue for the creation of graphene-based energy storage materials with improved performance potentially advancing the use of silicon-based anode materials in commercial applications.

CRediT authorship contribution statement

Fan Yang: Writing – original draft, Supervision, Project

administration, Methodology, Investigation, Funding acquisition, Conceptualization. **Pengcheng Deng:** Writing – original draft, Software, Methodology, Investigation, Data curation. **Hang He:** Writing – original draft, Software, Methodology, Investigation, Data curation, Conceptualization. **Ruolan Hong:** Investigation, Data curation. **Kun Xiang:** Investigation. **Yuan Cao:** Investigation, Data curation. **Beibei Yu:** Investigation. **Zeman Xie:** Investigation. **Jiming Lu:** Investigation. **Zikang Liu:** Investigation. **Danish Khan:** Writing – review & editing. **David Harbottle:** Writing – review & editing. **Zhenghe Xu:** Writing – review & editing. **Qingxia Liu:** Writing – review & editing, Resources, Funding acquisition. **Zeguo Tang:** Writing – review & editing, Investigation.

Declaration of competing interest

The authors declare that they have no known competing financial interests or personal relationships that could have appeared to influence the work reported in this paper.

Data availability

Data will be made available on request.

Acknowledgements

The work was supported by the National Natural Science Foundation of China (Grant No. 21808101), Natural Science Foundation for Top Talents of SZTU (Grant No. 20200207), Shenzhen Key Laboratory of Marine Energies and Environmental Safety (Grant No. ZDSYS2020121515400001), Pingshan District Innovation Platform Project of Shenzhen Hi-tech Zone Development Special Plan (Grant No. 29853M-KCJ-2023-002-02), Center for Frontier Science in Applied Surface and Interface Engineering (Grant No. 20201061020028), Leading Talents of Guangdong Province Program (Grant No. 2016LJ06C536).

Appendix A. Supplementary data

Supplementary data to this article can be found online at <https://doi.org/10.1016/j.cej.2024.152828>.

References

- [1] H. Zhang, et al., Graphite as anode materials: fundamental mechanism, *Recent Progr. Adv.* 36 (2021) 147–170.
- [2] A. Franco Gonzalez, N.-H. Yang, R.-S. Liu, Silicon anode design for lithium-ion batteries: Progress and perspectives, *J. Phys. Chem. C* 121 (50) (2017) 27775–27787.
- [3] L. Sun, et al., Recent progress and future perspective on practical silicon anode-based lithium ion batteries, *Energy Storage Mater.* 46 (2022) 482–502.
- [4] X. Meng, et al., Internal failure of anode materials for lithium batteries—a critical review, *Green Energy Environ.* 5 (1) (2020) 22–36.
- [5] C. Wang, et al., Anisotropic expansion and size-dependent fracture of silicon nanotubes during lithiation, *J. Mater. Chem. A* 7 (25) (2019) 15113–15122.
- [6] C.-B. Chang, et al., Solution-grown phosphorus-hyperdoped silicon nanowires/carbon nanotube bilayer fabric as a high-performance lithium-ion battery anode, *ACS Appl. Energy Mater.* 4 (4) (2021) 3160–3168.
- [7] B. Chen, et al., Space-confined atomic clusters catalyze superassembly of silicon nanodots within carbon frameworks for use in lithium-ion batteries, *Angew. Chem.* 132 (8) (2020) 3161–3166.
- [8] S.K. Kiran, et al., Silicon materials for lithium-ion battery applications, *Lithium-Ion Batteries: Mater. Appl.* 80 (2020) 161–202.
- [9] X. Dai, et al., Silicon nanoparticles encapsulated in multifunctional crosslinked nano-silica/carbon hybrid matrix as a high-performance anode for Li-ion batteries, *Chem. Eng. J.* 418 (2021) 129468.
- [10] J. Peng, et al., Si/C composite embedded nano-Si in 3D porous carbon matrix and enwrapped by conductive CNTs as anode of lithium-ion batteries, *Sustain. Mater. Technol.* 32 (2022) e00410.
- [11] S.-S. Lee, et al., Si-based composite interconnected by multiple matrices for high-performance Li-ion battery anodes, *Chem. Eng. J.* 381 (2020) 122619.
- [12] M. Jiang, et al., Assembly: A key enabler for the construction of superior silicon-based anodes, *Adv. Sci.* 9 (30) (2022) 2203162.
- [13] X. Li, et al., Research progress of silicon/carbon anode materials for lithium-ion batteries: structure design and synthesis method, *ChemElectroChem* 7 (21) (2020) 4289–4302.
- [14] S. Chae, et al., Integration of graphite and silicon anodes for the commercialization of high-energy lithium-ion batteries, *Angew. Chem. Int. Ed.* 59 (1) (2020) 110–135.
- [15] M. Ashuri, Q. He, L.L. Shaw, Improving cycle stability of Si anode through partially carbonized polydopamine coating, *J. Electroanal. Chem.* 876 (2020) 114738.
- [16] Q. Man, et al., Interfacial design of silicon/carbon anodes for rechargeable batteries: A review, *J. Energy Chem.* 76 (2023) 576–600.
- [17] F.H. Du, et al., Low-temperature synthesis of amorphous silicon and its ball-in-ball hollow nanospheres as high-performance anodes for sodium-ion batteries, *Adv. Mater. Interfaces* (2022) 2102158.
- [18] Y. Yao, et al., Interconnected silicon hollow nanospheres for lithium-ion battery anodes with long cycle life, *Nano Lett.* 11 (7) (2011) 2949–2954.
- [19] W. Tan, et al., A hierarchical Si/C nanocomposite of stable conductive network formed through thermal phase separation of asphaltene for high-performance Li-ion batteries, *Small* 18 (35) (2022) 2203102.
- [20] M. Piwko, et al., Hierarchical columnar silicon anode structures for high energy density lithium sulfur batteries, *J. Power Sources* 351 (2017) 183–191.
- [21] W. Kang, J.-C. Kim, D.-W. Kim, Waste glass microfiber filter-derived fabrication of fibrous yolk-shell structured silicon/carbon composite freestanding electrodes for lithium-ion battery anodes, *J. Power Sources* 468 (2020) 228407.
- [22] H. Zhao, et al., Si-based anodes: advances and challenges in li-ion batteries for enhanced stability, *Electrochem. Energy Rev.* 7 (1) (2024) 11.
- [23] I.Z. Gonzalez, et al., Silicon doped carbon nanotubes as high energy anode for lithium-ion batteries, *Mater. Today Commun.* 30 (2022) 103158.
- [24] Y. Wang, et al., Freestanding porous silicon@ heteroatom-doped porous carbon fiber anodes for high-performance Lithium-ion batteries, *ACS Appl. Energy Mater.* 5 (9) (2022) 11462–11471.
- [25] M. Choi, et al., A strategy of boosting the effect of carbon nanotubes in graphite-blended Si electrodes for high-energy lithium-ion batteries, *J. Storage Mater.* 72 (2023) 108301.
- [26] M. Choi, et al., Comparison of commercial silicon-based anode materials for the design of a high-energy lithium-ion battery, *Nano Res.* (2024) 1–8.
- [27] W. Luo, et al., Surface and interface engineering of silicon-based anode materials for lithium-ion batteries, *Adv. Energy Mater.* 7 (24) (2017) 1701083.
- [28] J. Guo, et al., Cyclability study of silicon–carbon composite anodes for lithium-ion batteries using electrochemical impedance spectroscopy, *Electrochim. Acta* 56 (11) (2011) 3981–3987.
- [29] J. Bi, et al., On the road to the frontiers of lithium-ion batteries: a review and outlook of graphene anodes, *Adv. Mater.* 35 (16) (2023) 2210734.
- [30] L. Dong, et al., A non-dispersion strategy for large-scale production of ultra-high concentration graphene slurries in water, *Nat. Commun.* 9 (1) (2018) 76.
- [31] Z. Song, et al., Intermolecular chemistry for designing functional binders in silicon/carbon composite anodes, *Mater. Today Energy* (2022) 101153.
- [32] V.L. Gurevich, M.I. Muradov, Release of the Joule heat upon passage of the electric current in nanostructures (a review), *Phys. Solid State* 54 (4) (2012) 663–681.
- [33] K.S. Varghese, et al., Technology, applications and modelling of ohmic heating: a review, *J. Food Sci. Technol.-Mysore* 51 (10) (2014) 2304–2317.
- [34] C. Huang, et al., Simultaneously bead-milled and reduced submicron silicon and graphene oxide for lithium storage, *J. Power Sources* 585 (2023) 233657.
- [35] G.P. Ojha, et al., Silicon carbide nanostructures as potential carbide material for electrochemical supercapacitors: A review, *Nanomaterials* 13 (1) (2022) 150.
- [36] M. Nolan, M. Legesse, G. Fagas, Surface orientation effects in crystalline–amorphous silicon interfaces, *Phys. Chem. Chem. Phys.* 14 (43) (2012) 15173–15179.
- [37] H. Yu, et al., A N-doped carbon nanocages@ silicon nanoparticles microcapsules for high-performance Li-storage, *Compos. B Eng.* 247 (2022) 110334.
- [38] J. Müller, et al., Effects of carbon coating on calendared nano-silicon graphite composite anodes of LiB, *J. Power Sources* 548 (2022) 232000.
- [39] X. Liu, et al., Electrolyte-philic and thermal-resistant polyimide separator enhances the performance of flexible silicon/carbon nanofibers for lithium-ion batteries, *J. Storage Mater.* 54 (2022) 105324.
- [40] R. Fu, et al., Graphene wrapped silicon suboxides anodes with suppressed Li-uptake behavior enabled superior cycling stability, *Energy Storage Mater.* 35 (2021) 317–326.
- [41] Y. Lu, et al., Graphene supported double-layer carbon encapsulated silicon for high-performance lithium-ion battery anode materials, *Carbon* 201 (2023) 962–971.
- [42] X. Kong, et al., Zinc oxide assisted synthesis of a holey carbon shell and graphene sheet supported silicon nanoparticle composite anode for lithium-ion batteries, *Compos. Commun.* 25 (2021) 100713.
- [43] Z. Li, et al., Covalent coating of micro-sized silicon with dynamically bonded graphene layers toward stably cycled lithium storage, *Adv. Energy Mater.* 13 (28) (2023) 2300874.
- [44] S. Xu, et al., In situ synthesis of graphene-coated silicon monoxide anodes from coal-derived humic acid for high-performance lithium-ion batteries, *Adv. Funct. Mater.* 31 (32) (2021) 2101645.
- [45] T. Mu, et al., Long-life silicon anodes by conformal molecular-deposited polyurea interface for lithium ion batteries, *Nano Energy* 103 (2022) 107829.
- [46] J. Xu, et al., Spheres of graphene and carbon nanotubes embedding silicon as mechanically resilient anodes for lithium-ion batteries, *Nano Lett.* 22 (7) (2022) 3054–3061.
- [47] W. Tan, et al., Fullerene-like elastic carbon coatings on silicon nanoparticles by solvent controlled association of natural polyaromatic molecules as high-

- performance lithium-ion battery anodes, *Energy Storage Mater.* 45 (2022) 412–421.
- [48] T. He, et al., Capacitive contribution matters in facilitating high power battery materials toward fast-charging alkali metal ion batteries, *Mater. Sci. Eng.: R: Reports* 154 (2023) 100737.
- [49] F. Yu, et al., Design and synthesis of electrode materials with both battery-type and capacitive charge storage, *Energy Storage Mater.* 22 (2019) 235–255.
- [50] H. Schichlein, et al., Deconvolution of electrochemical impedance spectra for the identification of electrode reaction mechanisms in solid oxide fuel cells, *J. Appl. Electrochem.* 32 (2002) 875–882.
- [51] T.H. Wan, et al., Influence of the discretization methods on the distribution of relaxation times deconvolution: implementing radial basis functions with DRTtools, *Electrochim. Acta* 184 (2015) 483–499.
- [52] P. Bai, M.Z. Bazant, Charge transfer kinetics at the solid–solid interface in porous electrodes, *Nat. Commun.* 5 (1) (2014) 3585.
- [53] F. Single, B. Horstmann, A. Latz, Theory of impedance spectroscopy for lithium batteries, *J. Phys. Chem. C* 123 (45) (2019) 27327–27343.
- [54] K. Pan, et al., Comprehensive electrochemical impedance spectroscopy study of Si-Based anodes using distribution of relaxation times analysis, *J. Power Sources* 479 (2020) 229083.
- [55] Y. He, et al., Progressive growth of the solid–electrolyte interphase towards the Si anode interior causes capacity fading, *Nat. Nanotechnol.* 16 (10) (2021) 1113–1120.
- [56] K. Zhang, et al., Review and stress analysis on the lithiation onset of amorphous silicon films, *Batteries* 9 (2) (2023) 105.
- [57] M. Gu, et al., Nanoscale silicon as anode for Li-ion batteries: The fundamentals, promises, and challenges, *Nano Energy* 17 (2015) 366–383.
- [58] Scaleup of FJH for graphene synthesis. see: <https://www.universalmatter.com/about-us/> (accessed 17 November 2022).
- [60] L. Li, et al., Nano-ordered structure regulation in delithiated Si anode triggered by homogeneous and stable Li-ion diffusion at the interface, *Nano Energy* 72 (2020) 104651.